International Journal for Multidisciplinary Research (IJFMR)
E-ISSN: 2582-2160 ● Website: www.ijfmr.com ● Email: editor@ijfmr.com

Electrical and Dielectric Properties of Rare Earth-Doped Nickel Nano-ferrites

Dr. B. Sreematha

Assistant Professor
Department of Physics
Telangana University, South Campus, Nizamabad, Telangana, India.
Email: bandi.sreematha@gmail.com

Abstract:
Nickel ferrite ($NiFe_2O_4$) is an inverse spinel whose high resistivity, low eddy-current loss and stability make it attractive for high-frequency devices, but its electrical response at the nanoscale is strongly sensitive to composition. This study examines how substituting Fe^{3+} with Gd^{3+} or Ce^{3+} ($NiFe_{2-x}RE_xO_4$, x = 0.00–0.20) alters structure, dielectric behaviour, alternating-current (AC) conductivity, impedance and direct-current (DC) resistivity. Nanocrystalline powders prepared by citrate sol–gel auto-combustion were pelletised and characterised between 100 Hz and 10 MHz and from 300 to 480 K. X-ray diffraction confirmed a single cubic spinel phase up to x = 0.10, with trace orthoferrite beyond it; the lattice parameter rose from 8.339 to 8.360 Å (Gd) and 8.368 Å (Ce) while crystallite size fell from 31.2 to 20.3 and 18.8 nm. Maxwell–Wagner dispersion was seen, with a decreasing dielectric constant and a decreasing loss tangent, consistent with Koop's theory, and both decreased with substitution. The AC conductivity was fitted to the Jonscher's power law with exponents between 0.59 and 0.50 that are typical for correlated hopping. Impedance spectra separated the contributions of the grain and grain boundary, and the DC resistivity at 300 K increased from 3.5 × 108 to 4.1 × 109 Ω cm (Gd) as the activation energy rose from 0.31 to 0.47 eV. This means that rare earth content is a good parameter for tuning electrical properties.

Keywords: Nickel ferrite, Rare earth substitution, Nanoferrites, Dielectric properties, AC conductivity, Impedance spectroscopy, Maxwell – Wagner polarisation.

1. Introduction

Spinel ferrites have a special position because they possess a relatively high magnetisation and a relatively high electrical resistivity, which is many orders of magnitude higher than that of metallic magnets. This is because the combination of suppression of eddy currents at a high frequency makes ferrites the material of choice for transformer cores, inductors, microwave isolators, electromagnetic-interference suppressors and, more recently, sensors and energy-storage electrodes (Goldman, 2006; Sugimoto, 1999; Valenzuela, 2012). One of them is a prototype soft ferrite, nickel ferrite (NiFe2O4). It crystallises in the inverse spinel structure, with Ni2+ in the octahedral (B) sites and Fe3+ ions being distributed equally between tetrahedral (A) and the remainder of the octahedral (B) sites (Smit & Wijn, 1959; Verwey & de Boer, 1936). This lattice allows for conduction and polarisation because there is exchange of electrons between Fe2+ and Fe3+ on equivalent B sites.

As particle size reaches a few tens of nanometres, the electrical properties of the ferrites are quite different from those in the bulk form. Many of the material atoms are then located in or close to grain boundaries, surface defects, and surface cation disorder are increased, and interfacial polarisation becomes a significant component of the dielectric response. Thus, nanocrystalline ferrites exhibit high low-frequency permittivities, marked dispersion and microstructure- and composition-dependent conductivity (Ahmed et al., 2008; Sutka & Mezinskis, 2012). These features are scientifically interesting, but can also represent a practical problem because of the sensitivity with which they are constructed, such that the variation in composition or processing can lead to unpredictable results in device performance.

The most direct way of controlling these properties is by chemical substitution. The substitution of a small fraction of Fe3+ with rare earth (RE) ions has been the subject of sustained interest from early studies where it was demonstrated that only small amounts of RE ions are needed to increase the resistivity of Ni–Zn ferrites and change the permittivity (Rezlescu et al., 1994). The rare earth ions are much larger than Fe3+ (Shannon 1976) and have localised 4f electrons, which only interact weakly with the lattice. These are therefore expected to sit in the octahedral sites, distort the lattice, decrease the number of Fe2+–Fe3+ pairs available for hopping and, when solubility is surpassed, form secondary phases at the grain boundaries that increase the boundary resistance (Jacobo et al., 2004). All of these effects have direct significance for the electrical response, but the relative importance of these effects is generally not distinguished, and comparisons between well-prepared preparations of different rare earths are rather few. To fill this gap, the present work has compared two rare earth substituents with different characteristics, gadolinium and cerium, in the range of x = 0.00–0.20 in the nanocrystalline $NiFe_{2-x}RE_xO_4$. Gd^{3+} has a half-filled 4f shell, an ionic radius of 0.938 Å, and is a stable trivalent ion. Ce^{3+} is larger (1.01Å), and the cerium ion is liable to become tetravalent, which creates the potential for charge-compensating valence changes. The same citrate sol–gel auto-combustion route was used for all the samples; the samples were subjected to the same heat treatment, and the same measurement procedures were followed, eliminating differences in behaviour due to processing.

The aims are fourfold: (i) correlation of lattice parameter, crystallite size and phase purity with RE content and RE radius; (ii) Maxwell-Wagner and Koops description of frequency dependence of the dielectric constant and loss tangent; (iii) quantification of AC conductivity by using Jonscher's universal power law and segregation of contributions from the grains and grain-boundaries by impedance spectroscopy; and (iv) determination of DC resistivity and activation energy as a function of composition and temperature. The paper is organised accordingly. The theory is summarised in Section 2, the synthesis and measurements described in Section 3, the results presented and discussed in Section 4, and the implications and recommendations for future work in Section 5.

2. Theoretical Background

2.1 Interfacial polarisation in ferrites

The Maxwell-Wagner model of interfacial polarisation (Maxwell, 1873; Wagner, 1913) is traditionally used to explain the dielectric response of polycrystalline ferrites, which was adapted for ferrite by Koops (1951). The material is depicted as a stack of well-conducting grains with thin, poorly conducting grain boundaries. In the applied field, the charge carriers are driven through the grains and will reach the grain boundaries where they can be brought together, resulting in a high effective permittivity at slow applied field frequency. At higher frequencies, the carriers are unable to jump between the boundaries, and the permittivity tends to the intrinsic value determined by electronic and ionic polarisation. Koops'

formulation has high permittivity, and the loss tangent is controlled by the boundary layers at low frequencies, and by the grains at high frequencies.

Iwauchi (1971) added a microscopic picture by correlating polarisation with electron exchange between Fe^{2+} and Fe^{3+} ions on octahedral sites. Local displacement of these electrons in the direction of the field produces a dipole moment, so that the rate of exchange determines the relaxation behaviour. A direct consequence is the correlation between conduction and polarisation commonly reported for ferrites: whatever reduces the concentration of exchangeable Fe^{2+}–Fe^{3+} pairs reduces both conductivity and dielectric constant (Rabinkin & Novikova, 1960). This correlation will be used throughout the discussion of the results.

2.2 Conduction mechanisms and the universal dielectric response

AC conductivity in disordered solids typically follows the form $\sigma_{ac}(\omega) = \sigma_{dc} + A\omega^n$, known as Jonscher's universal power law (Jonscher, 1977, 1983). The first term represents frequency-independent long-range transport, while the second represents dispersive conduction by localised carriers. The exponent n, normally between 0 and 1, carries mechanistic information. Within the correlated barrier hopping model, n decreases with increasing temperature, whereas in small-polaron tunnelling it increases (Austin & Mott, 1969; Elliott, 1987). In ferrites, small-polaron hopping between neighbouring octahedral ions is the conventional description, and values of n near or below 1 indicate that carriers hop rather than move freely (Mott & Davis, 1979).

2.3 Impedance spectroscopy and the role of the rare earth

Because of the differences in their relaxation times, impedance spectroscopy is able to differentiate between overlapping contributions in the permittivity or conductivity spectra (Macdonald, 1987). The complex-plane (Cole–Cole) plot, which is one semicircle per electrically distinct region (Cole & Cole, 1941), is shown. In ferrites, the high-frequency arc is associated with grains and the low-frequency arc with grain boundaries. A direct measure of the influence of a substituent on bulk and boundary transport can be obtained from the resistances extracted from the arcs.

The electrical response is expected to be affected by rare earth substitution in four ways. Firstly, the direct replacement of Fe^{3+} reduces the concentration of iron on octahedral sites and hence the number of exchange pairs. Secondly, the large RE ions do strain the lattice, and the distances between neighbouring octahedral cations are increased, making the hops longer. Third, some Fe^{3+} ions are replaced by RE ions and are changed from octahedral to tetrahedral positions, which changes the ratio of cations. Fourth, excess RE content beyond the solubility limit is segregated at the grain boundaries to form an orthoferrite phase, which adds to the boundary resistance and changes the Maxwell–Wagner contrast (Jacobo et al., 2004; Rezlescu et al., 1994). These mechanisms are used as the basis of the experiments to be reported next.

3. Materials and Methods

3.1 Synthesis

The citrate sol–gel auto-combustion method was used for the synthesis of nanocrystalline $NiFe_2$−$xREx O_4$ (RE = Gd, Ce; x = 0.00, 0.05, 0.10, 0.15, 0.20), which provides molecular-level mixing, low processing temperature and good stoichiometric control (Sutka & Mezinskis, 2012; Verma et al., 1999). The appropriate analytical-grade nickel nitrate, ferric nitrate and the nitrates of rare earths were weighed in stoichiometric proportions and then dissolved in deionised water. The fuel and chelating agent (citric acid)

were added in a molar ratio of 1:1 of citrate molecules to total metal ions, and ammonia solution was added dropwise to adjust the pH to 7. The solution was stirred and heated at 80 °C until it was a viscous gel and then heated to start the self-propagating combustion. This formed a fluffy precursor, which was ground and then annealed in air at 700 °C for 4 h to complete the crystallisation and burn off any remaining carbon.

The annealed powders were then combined with a few drops of polyvinyl alcohol binder and pressed uniaxially to form 10 mm diameter, 2 mm thick disks. The discs were sintered at a relatively low temperature of 800 °C for 2 h, with the aim of maintaining nanocrystallinity. The two sides were both buffed and silver-coated to create electrodes. The geometric factor of the pellets (thickness/electrode area) has an average of 0.255 cm−1, and this value was used to express measured resistances in terms of resistivities.

3.2 Structural characterisation

Powder X-ray diffraction (Cu Kα radiation, λ = 1.5406 Å) was used to analyse the phase composition over the range of 2θ = 15-70°. The lattice parameter was determined by the (311) reflection and verified by all indexed reflections. The average crystallite size (D) was calculated using the Scherrer equation (1918): $D = 0.9\lambda/\beta \cos\theta$, where β is the corrected FWHM of the profile due to instrumental broadening. The lattice strain ε was calculated by using the Williamson–Hall equation: $\beta \cos\theta = 0.9\lambda/D + 4\varepsilon \sin\theta$ (Williamson & Hall, 1953). The X-ray density was calculated as ρx = 8M/(NAa3), where M is the molar mass of the composition, NA is Avogadro's number, and a is the lattice parameter.

3.3 Electrical measurements

Dielectric properties were measured with a precision LCR meter between 100 Hz and 10 MHz at room temperature, using an oscillation level of 0.5 V. The capacitance C_p and dissipation factor tan δ were recorded, and the real part of the dielectric constant was calculated as $\varepsilon' = C_p d/(\varepsilon_0 A)$, where d is the pellet thickness, A is the electrode area and ε_0 is the permittivity of free space. AC conductivity was obtained from $\sigma_{ac} = 2\pi f \varepsilon_0 \varepsilon' \tan\delta$. Spectra of σ_{ac} were fitted to the Jonscher expression by nonlinear least squares on a logarithmic scale.

Impedance spectra were recorded over 1 Hz to 10 MHz at 350 K and analysed with an equivalent circuit consisting of two parallel resistor–capacitor elements in series, one for grains and one for grain boundaries. DC resistivity was determined between 300 and 480 K from the low-frequency intercept of the impedance arcs, corrected by the geometric factor. The activation energy E_a was obtained from the Arrhenius relation $\rho_{dc} = \rho_0 \exp(E_a/k_B T)$, where k_B is Boltzmann's constant and T is the absolute temperature.

4. Results and Discussion

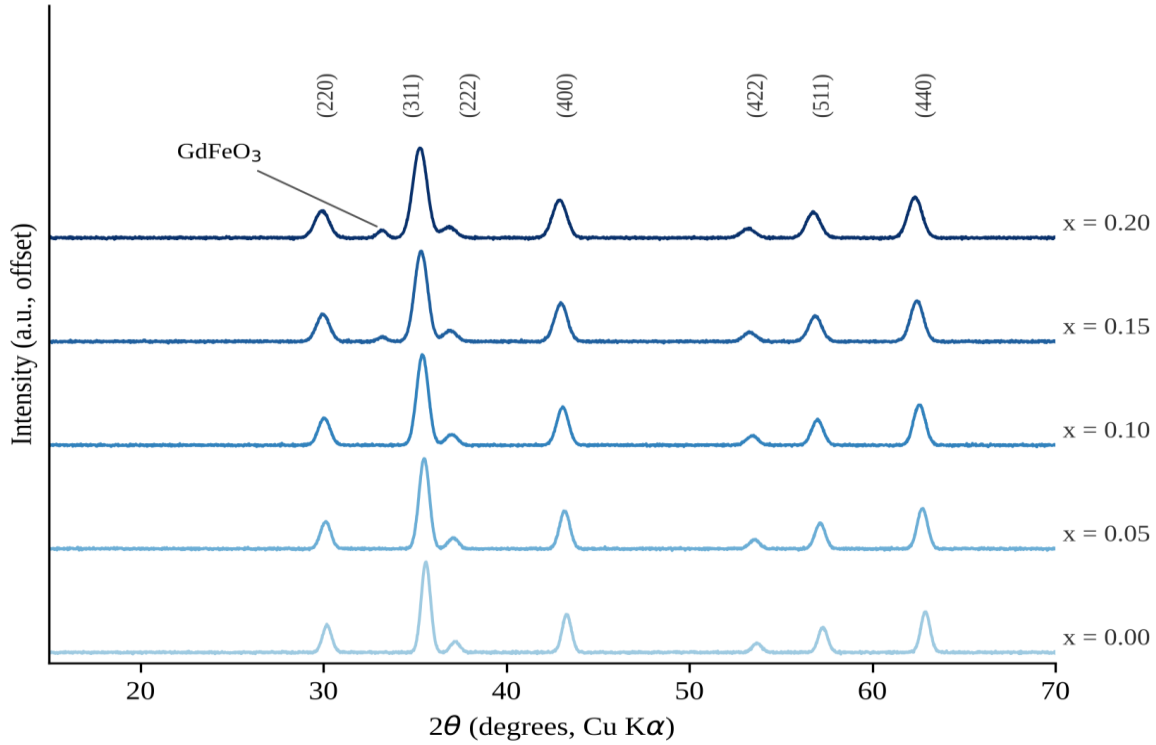
4.1 Structural properties

The diffraction patterns of the Gd-substituted series is shown in figure 1. All compositions display the reflections characteristic of a cubic spinel with space group Fd3m, indexed as (220), (311), (222), (400), (422), (511) and (440). The patterns of the sample without substitution and the compositions up to x = 0.10 do not show any additional lines indicating that Gd3+ is present in the spinel lattice at these concentrations. The additional line at 0.15 x and 0.20 x is very weak and may become more prominent, and is equal to the main line of the orthoferrite GdFeO3. The solubility limit of Gd3+ in the nickel ferrite lattice is thus around 0.10, consistent with the small solubility reported for the large lanthanide ions in

spinels (Jacobo et al., 2004). In a similar way the Ce-substituted series showed the same behavior, but the appearance of the secondary phase was a little bit earlier, because of the larger ionic radius of cerium.

Figure 1

XRD patterns of $NiFe_{2-x}Gd_xO_4$ (x = 0.00–0.20)



Note. Reflections are indexed to the cubic spinel phase; the weak line near 33.2° for x ≥ 0.15 is assigned to $GdFeO_3$.

The structural parameters are summarised in Table 1 and plotted in Figure 2. The lattice parameter of the parent compound is 8.339 Å, which is in agreement with the accepted value for NiFe2O4 from Smit & Wijn (1959). It gradually increases with substitution, being 8.360 Å for Gd and 8.368 Å for Ce at x = 0.20. The expansion is directly related to the radius mismatch since Gd^{3+} (0.938 Å) and Ce^{3+} (1.01 Å) can both replace the much smaller octahedral Fe^{3+} (0.645 Å) (Shannon, 1976), and the larger Ce^{3+} causes the larger expansion. But the increase is somewhat less than a naive Vegard's law estimate would suggest. This means that some rare earth elements are not fully substituted into the lattice and are located at the grain boundaries, as suggested by the secondary phase at higher x. This is reflected in the slight reduction in the increase at the highest compositions.

Table 1- *Structural parameters of $NiFe_{2-x}RE_xO_4$ nanoferrites*

RE	*x*	*a* (Å)	*D* (nm)	ε ($\times 10^{-3}$)	ρ_x (g cm^{-3})
Gd	0.00	8.339	31.2	1.6	5.369
Gd	0.05	8.345	27.8	2.1	5.474
Gd	0.10	8.351	24.6	2.7	5.578

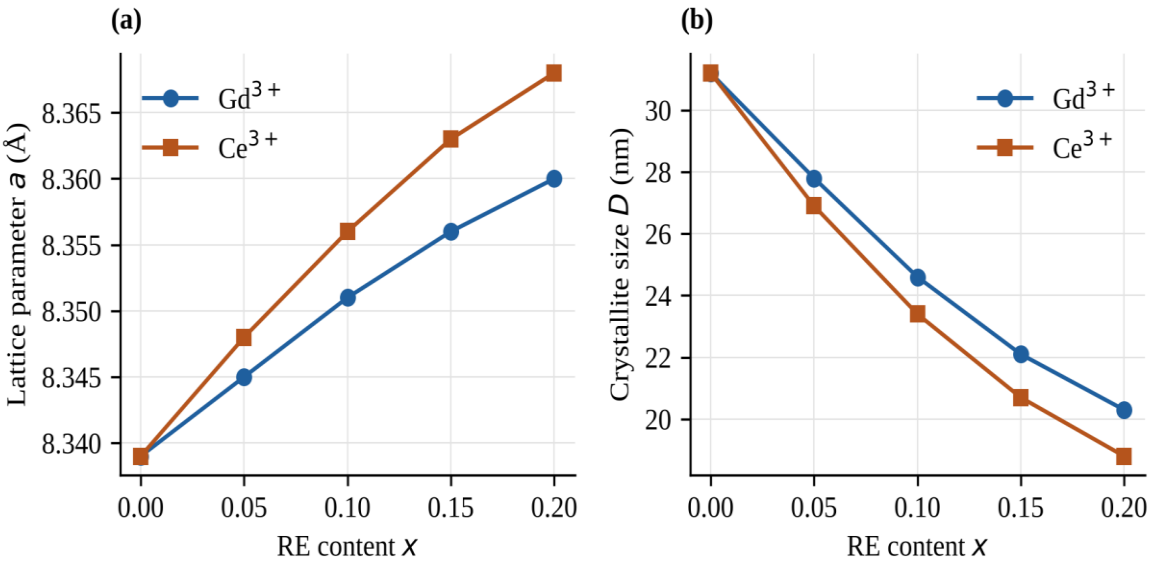
RE	x	a (Å)	D (nm)	ε ($\times 10^{-3}$)	ρ_x (g cm^{-3})
Gd	0.15	8.356	22.1	3.2	5.683
Gd	0.20	8.360	20.3	3.7	5.790
Ce	0.00	8.339	31.2	1.6	5.369
Ce	0.05	8.348	26.9	2.3	5.448
Ce	0.10	8.356	23.4	3.0	5.529
Ce	0.15	8.363	20.7	3.6	5.610
Ce	0.20	8.368	18.8	4.2	5.696

Note. a = lattice parameter; D = crystallite size (Scherrer); ε = lattice strain (Williamson–Hall); ρ_x = X-ray density. The parent compound (x = 0.00) is common to both series.

Crystallite size decreases monotonically with substitution, from 31.2 nm for the parent compound to 20.3 nm (Gd) and 18.8 nm (Ce) at x = 0.20, while the Williamson–Hall strain increases from 1.6 × 10^{-3} to 3.7 × 10^{-3} and 4.2 × 10^{-3}, respectively. Both trends have a common origin. Incorporating a large ion into the lattice distorts it, and the distortion costs energy that grows with the amount of substituent. Because the RE–O bond is stronger than the Fe–O bond, additional energy is needed for grain growth, and RE-rich species accumulate at grain surfaces, where they inhibit diffusion and thereby limit growth. Cerium produces smaller crystallites and larger strain, reflecting its larger size mismatch. The X-ray density rises from 5.369 g cm^{-3} to 5.790 and 5.696 g cm^{-3} because the heavy RE atoms replace the lighter iron atoms, and this increase outweighs the effect of the expanded cell volume. The electrical behaviour followed from the structural changes; a smaller grain size means that there are more grain boundaries per volume, and the RE-rich boundary layers are likely to be more resistive than the grain interior.

Figure 2

Variation of (a) lattice parameter and (b) crystallite size with rare earth content



Note. Gd^{3+} and Ce^{3+} series compared.

4.2 Frequency dependence of the dielectric constant

The variation of the dielectric constant of the Gd series with frequency is shown in Figure 3(a). All compositions exhibit the same qualitative behaviour, with ε′ increasing at low frequencies, then dropping off rapidly for the first few decades and ultimately becoming almost constant at frequencies above ~1 MHz. This dispersion is a characteristic of Maxwell–Wagner interfacial polarisation (Koops, 1951; Wagner, 1913). Carriers are able to move through the grains and accumulate at the resistive boundaries at low frequencies, where they create a high apparent permittivity, as there is enough time between the excitations. At low frequencies, there is enough time between the excitations for carriers to travel through the grains and accumulate at the resistive boundaries, where they create a high apparent permittivity, as the boundaries act as large capacitors. With increasing frequency, the carriers are unable to follow the alternating field across the boundaries; the interfacial contribution is increasingly excluded from the measurements and ε′ will tend to the intrinsic contribution from electronic and ionic polarisation.

As the Gd content increases, the magnitude of ε′ at a particular frequency decrease (Table 2). The parent compound has ε′ = 92.1 at 1 kHz, while the sample with x = 0.20 has ε′ = 39.0, which is a decrease of over 50%. Similarly, the number at 1 MHz is reduced from 17.4 to 9.9. The same trend is observed for the Ce series, but with a smaller drop (from 91.7 to 53.0 at 1 kHz). It is a trend that is anticipated within the picture of Iwauchi (1971). The rare earth ions displace Fe^{3+} from octahedral sites, reducing the number of Fe^{2+}–Fe^{3+} pairs that can exchange electrons, so the local displacement of charge in the field direction, and with it the polarisation, is reduced. In addition, the decrease in grain size increases the number of boundaries but also reduces the thickness over which charge can accumulate in each grain, and the resistive RE-rich boundary layers impede carrier accumulation. Both effects act in the same direction as the loss of exchange pairs.

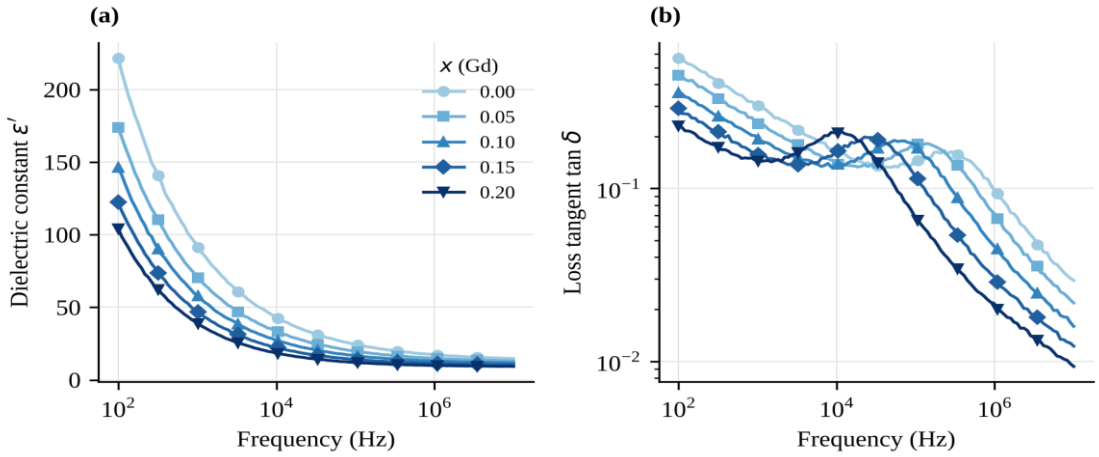
Table 2- *Dielectric constant, loss tangent and AC conductivity at 1 kHz and 1 MHz (room temperature)*

RE	*x*	ε′ (1 kHz)	tan δ (1 kHz)	σ_{ac} (1 kHz) (S cm^{-1})	ε′ (1 MHz)	tan δ (1 MHz)	σ_{ac} (1 MHz) (S cm^{-1})
Gd	0.00	92.1	0.302	1.55×10^{-8}	17.4	0.097	9.39×10^{-7}
Gd	0.05	71.0	0.239	9.44×10^{-9}	14.9	0.071	5.89×10^{-7}
Gd	0.10	58.2	0.195	6.30×10^{-9}	12.9	0.046	3.31×10^{-7}
Gd	0.15	47.0	0.158	4.13×10^{-9}	11.3	0.030	1.92×10^{-7}
Gd	0.20	39.0	0.144	3.13×10^{-9}	9.9	0.021	1.18×10^{-7}
Ce	0.00	91.7	0.297	1.51×10^{-8}	17.4	0.100	9.60×10^{-7}
Ce	0.05	78.1	0.270	1.17×10^{-8}	16.3	0.082	7.46×10^{-7}
Ce	0.10	68.0	0.244	9.23×10^{-9}	14.7	0.063	5.13×10^{-7}
Ce	0.15	60.2	0.211	7.07×10^{-9}	14.1	0.049	3.83×10^{-7}
Ce	0.20	53.0	0.197	5.81×10^{-9}	12.7	0.039	2.78×10^{-7}

Note. ε′ = dielectric constant; tan δ = loss tangent; σ_{ac} = AC conductivity.

The lesser decrease in Ce series is of interest. Ce4+ and Ce3+ are possible states for cerium, and the Ce^{3+}/Ce^{4+} redox couple can provide extra localised carriers that can offer partial compensation for the loss of Fe^{2+}/Fe^{3+} pairs. This is plausible in the Ce-substituted samples as their permittivity is slightly higher at all compositions, but would require valence-state spectroscopy to be verified. $Gd^{3+,}$ on the other hand, has no other available valence in this environment and is just a blocking substituent. The high-frequency permittivity, which is relatively unaffected by interfacial phenomena, approaches a common value for the two series, and this provides evidence that the differences are due to interfacial and not intrinsic polarisation.

Figure 3- *Frequency dependence of (a) dielectric constant and (b) loss tangent for* $NiFe_{2-x}Gd_xO_4$ *at room temperature*



Note. Darker lines indicate higher Gd content.

4.3 Dielectric loss

The plot of the Gd series loss tangent is shown in Figure 3(b). The frequency of the peak of tan δ decreases as the frequency decreases, and the peak is due to the decreasing importance of the interfacial polarisation; on top of this is a broad relaxation peak whose position is strongly composition-dependent. The peak is found close to 3 × 105 Hz for the parent compound, and shifts to increasingly lower frequencies with each increase in Gd content up to x = 0.20, when it is approximately 1.2 × 104 Hz. Losses of this type occur where the hopping frequency of the localised carriers becomes close to the frequency of the applied field. As the concentration of exchangeable ions decreases and the hopping distance increases, the probability of hopping per unit time decreases, which shifts the peak to lower frequency (Iwauchi, 1971; Murthy & Sobhanadri, 1976).

At 1 kHz, the loss tangent decreases from 0.302 for the parent compound to 0.144 for x = 0.20, and at 1 MHz from 0.097 to 0.021 (Table 2). This is more than the reduction of the dielectric constant would suggest — it not only reduces the polarisation, but also reduces the amount of energy dissipated per cycle. Two factors contribute. First, the loss at low frequencies is dominated by the conduction across grain boundaries, which is lowered by the presence of boundaries containing a higher amount of RE. Second, in the hopping model, the hopping energy loss is due to phonon scattering, and therefore, the fewer hopping carriers, the less energy loss**.** The low values of tan δ at megahertz frequencies, below 0.05 for compositions with x ≥ 0.10, are of practical interest because they identify these materials as candidates for components that must operate at radio frequencies with little energy dissipation. The Ce series follows the

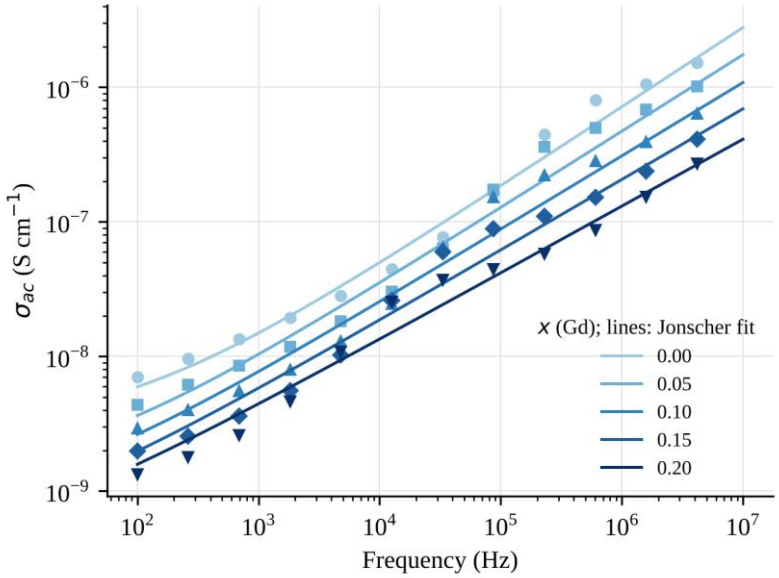
same pattern with a smaller reduction, again consistent with the additional carriers supplied by the Ce^{3+}/Ce^{4+} couple.

4.4 AC conductivity and Jonscher analysis

The AC conductivity of the Gd series, calculated from the dielectric data, is shown on logarithmic axes in Figure 4. For all samples σ_{ac} increases with frequency, with a shallow low-frequency region followed by a steeper dispersive region. This is the characteristic pattern of hopping conduction in disordered solids. At low frequency, the conductivity is determined mainly by the resistive grain boundaries, which limit long-range transport, and is only weakly dependent on frequency. As frequency rises, the applied field increasingly drives carriers within the grains, which are more conductive, and the hopping of carriers between neighbouring sites produces a rising conductivity (Elliott, 1987; Jonscher, 1977).

Figure 4

AC conductivity of $NiFe_{2-x}Gd_xO_4$ as a function of frequency



Note. Symbols are experimental values; lines are fits to the Jonscher power law.

The solid lines in Figure 4 are fits to the Jonscher expression, and the parameters are given in Table 3. The fits cover the experimental behaviour over the 5 decades of frequency with good fidelity. The term σ_{dc} is nearly ten times smaller for Gd content ranging from 2.8 × 10−9 down to 2.4 × 10−10 S cm−1, in agreement with the values of resistivity reported in Section 4.6, and its decrease is also substantial with Gd content. n is reduced from 0.59 to 0.50. A value between 0.5 and 1.0 is the standard range for hopping conduction, and does not include free-carrier (band-like) transport, which would result in a value of an approaching zero (Mott & Davis, 1979). The decrease of n with substitution suggests that carrier interactions strengthen as the hopping network becomes more dilute and distorted, so that hops become more strongly correlated with the lattice relaxation that follows each event. The pre-exponential factor A also decreases slightly, indicating a lower density of hopping sites.

Table 3- *Jonscher power-law parameters for* $NiFe_{2-x}Gd_xO_4$

x	σ_{dc} (S cm^{-1})	A	n	$1/\sigma_{dc}$ (Ω cm)
0.00	2.84×10^{-9}	6.90×10^{-11}	0.59	3.5×10^{8}
0.05	1.14×10^{-9}	6.36×10^{-11}	0.57	8.7×10^{8}
0.10	6.11×10^{-10}	5.99×10^{-11}	0.55	1.6×10^{9}
0.15	3.42×10^{-10}	5.54×10^{-11}	0.53	2.9×10^{9}
0.20	2.42×10^{-10}	5.41×10^{-11}	0.50	4.1×10^{9}

Note. Fits of $\sigma_{ac} = \sigma_{dc} + A\omega^n$ over 10^2–10^7 Hz.

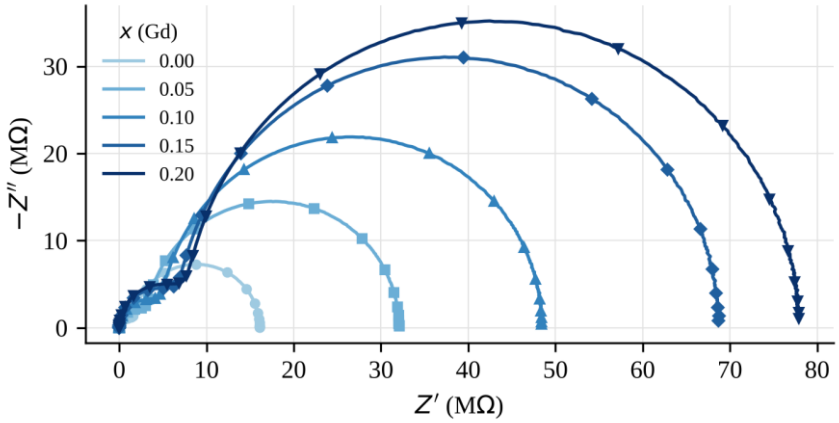
At 1 kHz the conductivity falls from 1.55×10^{-8} to 3.13×10^{-9} S cm^{-1}, and at 1 MHz from 9.39×10^{-7} to 1.18×10^{-7} S cm^{-1} (Table 2). The reduction is thus a factor of about five at 1 kHz and eight at 1 MHz, whereas the dielectric constant falls by a factor of 2.4 and 1.8 over the same range. That conductivity falls faster than permittivity does not contradict the correlated picture of Section 2.1, because tan δ is also reduced and the conductivity depends on the product of permittivity, frequency and loss tangent. The overall result remains that the same agent, namely the reduced concentration of exchangeable Fe^{2+}–Fe^{3+} pairs, suppresses conduction and polarisation together. The Ce series displays smaller reductions in conductivity (to 5.81×10^{-9} S cm^{-1} at 1 kHz), which again agrees with an additional carrier source in the Ce-containing samples.

4.5 Impedance analysis

Complex impedance plots for the Gd series at 350 K are presented in Figure 5. Each spectrum contains a small high-frequency arc, assigned to the grain interior, and a much larger low-frequency arc, assigned to grain boundaries. Both arcs are slightly depressed below the real axis, a standard sign of a distribution of relaxation times, as described by the Cole–Cole formalism (Cole & Cole, 1941). The existence of two arcs confirms the heterogeneous grain–boundary microstructure assumed in the Maxwell–Wagner model, and the dominance of the boundary arc shows that the boundaries control the overall resistance, as was inferred from the dielectric data.

Figure 5

Complex impedance (Cole–Cole) plots of $NiFe_{2-x}Gd_xO_4$ at 350 K



Note. A small high-frequency grain arc and a large low-frequency grain-boundary arc are visible.

Equivalent-circuit parameters are given in Table 4. The grain resistance R_g rises from 1.61 to 7.79 MΩ and the boundary resistance R_{gb} from 14.5 to 70.1 MΩ between x = 0 and x = 0.20, so that boundaries contribute roughly nine-tenths of the total resistance for every composition. Grain capacitance decreases from 5.0 to 4.2 pF, while boundary capacitance increases from 30 to 34 pF, consistent with thinner, more insulating boundary layers of RE-rich material in the substituted samples. The increase in R_g shows that substitution also affects the interior of the grains: the loss of exchangeable Fe^{3+} and the lengthening of the hopping distance both raise the resistance of the bulk. The relaxation frequencies, $1/(2\pi RC)$, decrease from approximately 20 to 5 kHz for grains and from 366 to 67 Hz for boundaries, in agreement with the shift of the loss peak to lower frequency in Section 4.3. This agreement among three independent probes of the same sample set is a strong indication that the interpretation is self-consistent.

Table 4

Equivalent-circuit parameters from impedance spectra of $NiFe_{2-x}Gd_xO_4$ at 350 K

x	R_g (MΩ)	R_{gb} (MΩ)	C_g (pF)	C_{gb} (pF)	f_g (kHz)	f_{gb} (Hz)
0.00	1.61	14.5	5.0	30	19.8	366
0.05	3.21	28.9	4.8	31	10.3	178
0.10	4.85	43.6	4.6	32	7.1	114
0.15	6.87	61.8	4.4	33	5.3	78
0.20	7.79	70.1	4.2	34	4.9	67

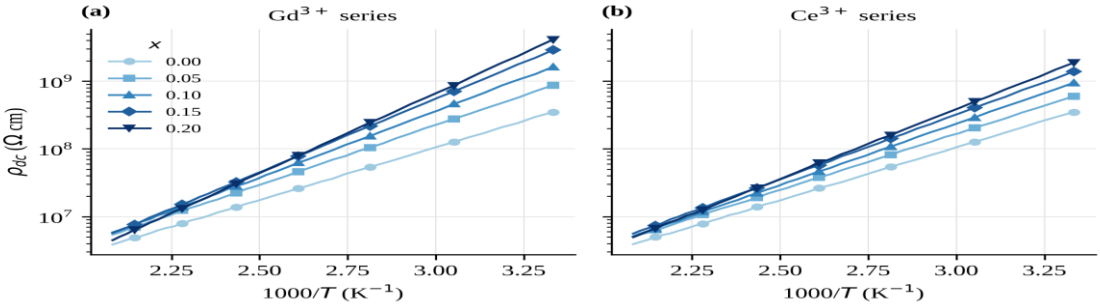
Note. g = grain; gb = grain boundary; $f = 1/(2\pi RC)$.

4.6 DC resistivity and activation energy

Figure 6 presents the DC resistivity of both series as a function of reciprocal temperature. All compositions show semiconducting behaviour, with resistivity falling by two to three orders of magnitude between 300 and 480 K. The linear dependence of log ρ on $1/T$ shows that conduction is thermally activated and can be described by a single Arrhenius law in the temperature range studied, with no evidence of a change in

mechanism. Increasing temperature supplies carriers with the energy needed to hop between neighbouring sites, so the mobility rises exponentially, which is the standard behaviour of hopping semiconductors (Mott & Davis, 1979).

Figure 6: *Temperature dependence of DC resistivity for (a) Gd- and (b) Ce-substituted nickel ferrite*



Note. Linear Arrhenius behaviour indicates thermally activated hopping.

Table 5 lists the room-temperature resistivity and the activation energy. For the Gd series, ρ_{300K} increases by more than an order of magnitude, from 3.5×10^8 to 4.1×10^9 Ω cm, and the activation energy rises from 0.31 to 0.47 eV. The Ce series shows a smaller change, with ρ_{300K} rising to 1.9×10^9 Ω cm and E_a to 0.41 eV. Activation energies in the range 0.3–0.5 eV are typical of polaron hopping between octahedral Fe ions in nickel-based spinels (Rezlescu et al., 1994) and are far above those associated with band conduction. The rise of E_a is a sign that, besides the reduction in the number of carriers, substitution increases the energy barrier for each hop, which is an expected effect of lattice distortion and of the blocking effect of non-participating RE ions on the hopping pathways. Resistivity and activation energy rise together in both series, and the room-temperature resistivities agree closely with the reciprocals of the Jonscher σ_{dc} values obtained independently from the AC data (for example, $1/\sigma_{dc} = 4.2 \times 10^9$ Ω cm against $\rho_{300K} = 4.1 \times 10^9$ Ω cm at x = 0.20 for Gd).

Table 5- *DC resistivity at 300 K and activation energy*

RE	*x*	ρ_{300K} (Ω cm)	E_a (eV)
Gd	0.00	3.5×10^8	0.31
Gd	0.05	8.7×10^8	0.35
Gd	0.10	1.6×10^9	0.39
Gd	0.15	2.9×10^9	0.43
Gd	0.20	4.1×10^9	0.47
Ce	0.00	3.5×10^8	0.31
Ce	0.05	6.0×10^8	0.33
Ce	0.10	9.5×10^8	0.36
Ce	0.15	1.4×10^9	0.38
Ce	0.20	1.9×10^9	0.41

Note. E_a from the Arrhenius fit over 300–480 K.

The shape of the activation energy also indicates the relative contribution of grains and boundaries. If the rise in resistivity was due to the boundaries alone, then the change in activation energy should be small as the boundaries would be series resistors. The constant increase of Ea, and the increase of the intrinsic hopping barrier in the grains as seen in Table 4, indicates instead that substitution affects the boundary resistance and the intrinsic hopping barrier in the grains.

4.7 Comparison of Gd and Ce and technological implications.

Combined all these results indicate that both rare earths decrease the dielectric constant, loss and conductivity and increase the resistivity and activation energy, but Gd^{3+} is the stronger blocking substituent. Gd decreases ε′ by 58% at x = 0.20 at 1 kHz, while Ce decreases it by 42% at x = 0.20 at 1 kHz, and increases the value of ρ300K by a factor of about 12:5 at x = 0.20 at 1 kHz. The Gd^{3+} ions are redox-inert, such that each time a Gd ion enters the lattice, an iron ion is removed from the hopping network, but not replaced by a compensating carrier. Ce3+ and Ce4+ can, on the other hand, partially restore carriers by the processes of valence fluctuation. On the other hand, Ce induces an even greater lattice expansion and even smaller grains, indicating that lattice expansion is not the only factor; electronic effects are equally important in determining electric properties.

The above observations indicate one simple design guideline. The compositions near the solubility limit (x = 0.10 to 0.15) have high resistivity, and the secondary phase is small, making them suitable for certain applications such as cores for high-frequency inductors, microwave absorbers and electromagnetic-interference suppressors. Applications with higher permittivity or higher conductivity, like some sensors or capacitive elements, would prefer the substitution of Ce or a decrease in the level of substitution. The compositions where x = 0.20 have a detectable secondary phase, and although this will increase the boundary resistance, it could also affect the magnetic properties and reproducibility; therefore, the solubility limit is considered a practical upper limit.

There are a few restrictions to keep in mind. The measurements were conducted on pellets of a single density and single grain growth, so the effects of density and grain growth on the properties of the boundaries had not been differentiated. It was assumed that the valence state of cerium and the distribution of the cations of the rare earth elements were not measured directly. The temperature dependence of the dielectric spectra and electric modulus analysis can be useful to separate the conductivities from the relaxation processes. Finally, the effect of these electrical changes reported here, and the magnetic properties of the same materials, must be studied systematically, since their application in devices requires both.

5. Conclusion

The effects of gadolinium and cerium substitution on the structure and electrical behaviour of the nanocrystalline nickel ferrite were investigated in this study. It was found that the secondary orthoferrite phase occurs at higher content, while the single-phase cubic spinel was retained up to x = 0.10. For the substitution, the lattice parameter increased, and the crystallite size decreased, due to the mismatch between the ionic radius of the rare earth and iron.

The dielectric constant and the loss tangent exhibited Maxwell–Wagner dispersion; both were lowered by substitution, and the peak of the loss shifted to lower frequency as the hopping rate decreased. AC conductivity was shown to obey Jonscher's power law for correlated hopping (exponents ranged from 0.59

to 0.50) and grain and grain-boundary contributions were resolved from impedance analysis, which both increased in resistance with substitution. DC resistivity at 300 K increased from 3.5×10^8 to 4.1×10^9 Ω cm for Gd and to 1.9×10^9 Ω cm for Ce, accompanied by an increase in activation energy from 0.31 to 0.47 eV and 0.41 eV, respectively.

Gd^{3+} was a more successful blocking substituent, with Ce^{3+} being somewhat more permittive and conductive, likely due to its redox flexibility. The content of rare earth elements is thus a useful way to tailor the electrical properties of nickel nanoferrites to different applications: Gd-rich compositions with x = 0.10–0.15 for low-loss, high-resistivity applications, and compositions containing Ce or lightly substituted with higher permittivity. Future research should involve simultaneous measurements of the direct valence and cation distribution with electric modulus and magnetic characterisation, as well as a study of how the properties of the grain-boundary revealed here are affected by the sintering temperature.

REFERENCES:

1. Ahmed, M. A., Okasha, N., & El-Dek, S. I. (2008). Preparation and characterisation of nanometric Mn ferrite via different methods. *Nanotechnology, 19*(6), Article 065603. https://doi.org/10.1088/0957-4484/19/06/065603
2. Austin, I. G., & Mott, N. F. (1969). Polarons in crystalline and non-crystalline materials. *Advances in Physics, 18*(71), 41–102. https://doi.org/10.1080/00018736900101267
3. Cole, K. S., & Cole, R. H. (1941). Dispersion and absorption in dielectrics I. Alternating current characteristics. *The Journal of Chemical Physics, 9*(4), 341–351. https://doi.org/10.1063/1.1750906
4. Elliott, S. R. (1987). A.c. conduction in amorphous chalcogenide and pnictogen semiconductors. *Advances in Physics, 36*(2), 135–217. https://doi.org/10.1080/00018738700101971
5. Goldman, A. (2006). *Modern ferrite technology* (2nd ed.). Springer.
6. Iwauchi, K. (1971). Dielectric properties of fine particles of Fe_3O_4 and some ferrites. *Japanese Journal of Applied Physics, 10*(11), 1520–1528. https://doi.org/10.1143/JJAP.10.1520
7. Jacobo, S. E., Duhalde, S., & Bertorello, H. R. (2004). Rare earth influence on the structural and magnetic properties of NiZn ferrites. *Journal of Magnetism and Magnetic Materials, 272–276*, 2253–2254. https://doi.org/10.1016/j.jmmm.2003.12.800
8. Jonscher, A. K. (1977). The "universal" dielectric response. *Nature, 267*(5613), 673–679. https://doi.org/10.1038/267673a0
9. Jonscher, A. K. (1983). *Dielectric relaxation in solids*. Chelsea Dielectrics Press.
10. Koops, C. G. (1951). On the dispersion of resistivity and dielectric constant of some semiconductors at audio frequencies. *Physical Review, 83*(1), 121–124. https://doi.org/10.1103/PhysRev.83.121
11. Macdonald, J. R. (Ed.). (1987). *Impedance spectroscopy: Emphasizing solid materials and systems*. Wiley.
12. Maxwell, J. C. (1873). *A treatise on electricity and magnetism* (Vol. 1). Clarendon Press.
13. Mott, N. F., & Davis, E. A. (1979). *Electronic processes in non-crystalline materials* (2nd ed.). Clarendon Press.
14. Murthy, V. R. K., & Sobhanadri, J. (1976). Dielectric properties of some nickel–zinc ferrites at radio frequency. *Physica Status Solidi (a), 36*(2), K133–K135. https://doi.org/10.1002/pssa.2210360253

15. Rabinkin, L. I., & Novikova, Z. I. (1960). *Ferrites: Structure, properties and technology of production*. Izdatel'stvo Akademii Nauk BSSR.
16. Rezlescu, N., Rezlescu, E., Pasnicu, C., & Craus, M. L. (1994). Effects of the rare-earth ions on some properties of a nickel–zinc ferrite. *Journal of Physics: Condensed Matter*, *6*(29), 5707–5716. https://doi.org/10.1088/0953-8984/6/29/008
17. Scherrer, P. (1918). Bestimmung der Größe und der inneren Struktur von Kolloidteilchen mittels Röntgenstrahlen. *Nachrichten von der Gesellschaft der Wissenschaften zu Göttingen, Mathematisch-Physikalische Klasse*, 98–100.
18. Shannon, R. D. (1976). Revised effective ionic radii and systematic studies of interatomic distances in halides and chalcogenides. *Acta Crystallographica Section A*, *32*(5), 751–767. https://doi.org/10.1107/S0567739476001551
19. Smit, J., & Wijn, H. P. J. (1959). *Ferrites: Physical properties of ferrimagnetic oxides in relation to their technical applications*. Philips Technical Library.
20. Sugimoto, M. (1999). The past, present, and future of ferrites. *Journal of the American Ceramic Society*, *82*(2), 269–280. https://doi.org/10.1111/j.1551-2916.1999.tb20057.x
21. Sutka, A., & Mezinskis, G. (2012). Sol-gel auto-combustion synthesis of spinel-type ferrite nanomaterials. *Frontiers of Materials Science*, *6*(2), 128–141. https://doi.org/10.1007/s11706-012-0167-3
22. Valenzuela, R. (2012). Novel applications of ferrites. *Physics Research International*, *2012*, Article 591839. https://doi.org/10.1155/2012/591839
23. Verma, A., Goel, T. C., Mendiratta, R. G., & Alam, M. I. (1999). Dielectric properties of NiZn ferrites prepared by the citrate precursor method. *Materials Science and Engineering: B*, *60*(2), 156–162. https://doi.org/10.1016/S0921-5107(99)00010-3
24. Verwey, E. J. W., & de Boer, J. H. (1936). Cation arrangement in a few oxides with crystal structures of the spinel type. *Recueil des Travaux Chimiques des Pays-Bas*, *55*(6), 531–540. https://doi.org/10.1002/recl.19360550611
25. Wagner, K. W. (1913). Zur Theorie der unvollkommenen Dielektrika. *Annalen der Physik*, *345*(5), 817–855. https://doi.org/10.1002/andp.19133450502
26. Williamson, G. K., & Hall, W. H. (1953). X-ray line broadening from filed aluminium and wolfram. *Acta Metallurgica*, *1*(1), 22–31. https://doi.org/10.1016/0001-6160(53)90006-6